NATIONAL AIR INTELLIGENCE CENTER

SELECTED ARTICLES
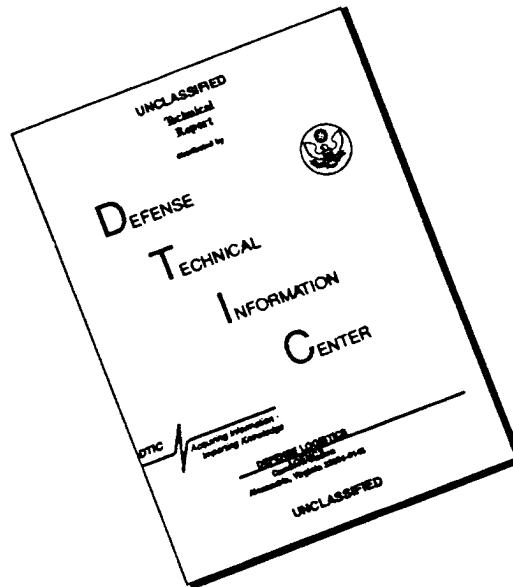
DTIC QUALITY INSPECTED 4

19960619 011

DISCLAIMER NOTICE

THIS DOCUMENT IS BEST QUALITY AVAILABLE. THE COPY FURNISHED TO DTIC CONTAINED A SIGNIFICANT NUMBER OF PAGES WHICH DO NOT REPRODUCE LEGIBLY.

HUMAN TRANSLATION

NAIC-ID(RS)T-0137-96   2 May 1996

MICROFICHE NR: 96C000364

SELECTED ARTICLES

English pages: 38

Source: Qiangjiguang Yu Lizishu (High Power Laser and Particle
           Beams), Vol.4, Nr. 1, February 1992; pp. 59-70; 86-92

Country of origin: China
Translated by: Leo Kanner Associates
               F33657-88-D-2188
Requester: NAIC/TATD/Bruce Armstrong
Approved for public release: distribution unlimited.

TABLE OF CONTENTS

GRAPHICS DISCLAIMER

All figures, graphics, tables, equations, etc. merged into this
translation were extracted from the best quality copy available.

EFFECTS OF MIRROR COATING-THICKNESS NONUNIFORMITIES ON POLARIZATION AND OPTICAL-FIGURE PROPERTIES OF LASER AND BEACON LIGHT

Xiong Shengming and Zhang Yundong

Institute of Optics and Electronics
Chinese Academy of Sciences
P.O. Box 350
Shuangliu, Chengdu 610209

ABSTRACT This paper discusses mirror coating nonuniformities caused by geometrical constraints in the chamber used and their effects on polarization of light beams for enhanced metal coatings. Phase distortions of $1.06-\mu m$ laser beam and $0.5893-\mu m$ beacon beam have been calculated. Phase distortions with same signs have been obtained using a modified design.

KRY WORDS coating thickness nonuniformities , polarization, phase distortion.

I. Introduction

The mirror diameter is D at the beginning terminal of a high-power laser. Based on considerations of Gaussian light beams, at the beam waist the divergence angle θ is approximately equal to λ/D (λ is the laser wavelength). Also, consideration is given to thermal blooming generated by a high-power laser in atmospheric propagation, and to other nonlinear optical effects, such as stimulated Raman scattering; it is required that the mirror

1

diameter D should be large at the beginning terminal. In a practical high-power laser emission system, the mirror diameter is generally between 5 and 20m. A large-diameter reflective mirror is not only difficult to machine, but is also high in cost. Additionally, depositing a thin coating on this large mirror surface, especially the uniformity of coating layer thickness distribution, is very important and difficult. Nonuniform deposition leads to polarization aberrations and wavefront anomalies, thus affecting far field diffraction properties [1].

Another important problem in a high-power laser system is the presence of many factors leading to optical wavefront errors in the optical passage so that the light beam energy is scattered. Thus, compensations should be made with adaptive-optics technology. However, an appropriate light source should be the information carrier of the wavefront errors for light from the source in order to compensate for these errors. Such light is usually called a beacon light.

After the light beam bounces back from the reflective mirrors of different coating systems, phase shifts will be generated. Light at different wavelengths undergo different phase shifts. However, due to the nonuniformity of coating thickness, phase anomalies are generated. With respect to light at different wavelengths, phase anomalies are different, even generating phase anomalies with sign reversal. Then, compensating with a beacon light may yield reverse results, failing to attain the expected purposes.

From the available conditions, this article takes into account the geometric constraints in the film-coating chamber in calculating the coating-thickness distribution of a nearly-spherical surface reflective mirror with 0.8m diameter in order to attain optimization. In the case of the metal-enhanced type high-reflectivity mirror system of this distribution, with respect to the phase anomalies generated by a 1.06μm primary laser and a 0.5893μm beacon light, and with the modified coating system, the design is so executed that the phase anomaly signs at both wavelengths are consistent.

II. Effect of Physical Constraints in Film-coating Device on Coating-Thickness Uniformity

Two kinds of uniformity should be of concern to us for coatings on large reflective mirrors: one is orientational uniformity and the other is diametral uniformity. Orientational uniformity can be very easily attained by high-speed rotation of the reflective mirror, or compensated with a ring vapor source. Fig. 1 shows the ring vapor source. With regard to large reflective mirrors, for safety reasons generally low-speed rotation was employed. Therefore, it was necessary to use a ring source apparatus for good orientational uniformity. However, diametral coating-thickness distribution was difficult to control. Diametral coating-thickness distribution relied on three parameters[2]:
(1) the f-value of an optical reflective mirror and surface aspherical shape; (2) vapor source-to-substrate distance H;
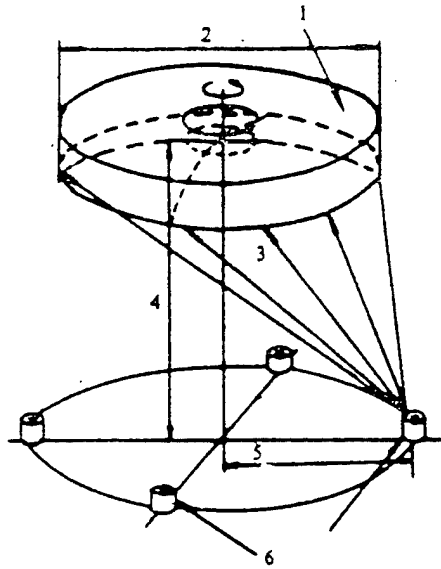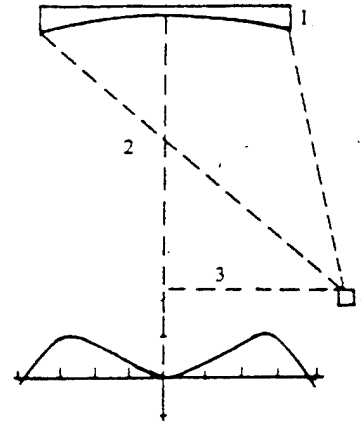
3

Fig.1 Ring source coating geometry using a series of vapor source arranged to simulate a ring vapor source of diameter 2D placed underneath a rotating primary mirror.
1.rotating primary mirror
2.mirror diameter D_t
3.vapor stream
4.source - to - subtrate distance H
5.source offset D 6. vapor source

Fig.2 Optimized coating thickness uniformity for 0.8 meter diameter $F/2.0$ concave mirror.
1.mirror   2.optimum source - to - substrate height $H = 0.9$m   3.optimum offset $D = 0.63$m
4.vapor source

Radial distance (m)

and (3) distance D (offset) of the vapor source relative to the rotational center of the reflective mirror. With respect to the spherical-surface rotation fixture, the coating thickness relationship at any point P on the substrate is:

$$t_{sp} = \frac{mh}{\mu\pi} \cdot \frac{[(h^2 + D^2 - \rho^2)(h\cos A + \rho\sin A) - 2\rho D^2 \sin A]}{[h^2 + (D+\rho)^2]^{1/2} \cdot [h^2 + (D-\rho)^2]^{3/2}} \tag{1}$$

In the equation
$$h = H - R(1 - \cos A) \tag{2}$$

$$\sin A = \frac{\rho}{R} \tag{3}$$

In the above equations, m is the total quantity of evaporated

4

material; μ is density; R is the spherical-surface radius; ρ is the ratio between the t_{sp} (relative thickness) and thickness t_{so} in Eq. (1) when ρ=0, from point P to the diametral radius of the axis of rotation.

Fig. 2 indicates the optimal coating-thickness condition for a reflective mirror with F/2.0, and an 0.8m-diameter. From this figure we can see that the height of the film-coating apparatus housing had to be 1.3m and the diameter had to be 1.5m for uniformity below 0.5% with the vapor source-to-substrate distance H 0.9m and the offset 0.3m. However, the equipment available to us could not satisfy these requirements. Due to reasons of cost, remodeling of the available equipment was necessary; thus, ideal coating-thickness uniformity could not be realized. Fig. 3 indicates the effect of offset D on coating-thickness uniformity with known height H. From the figure, for H at 0.65m, for uniformity of ±1.5%, the offset was required to be between 0.48m and 0.5m. However, our available coating machine was 1.5m in diameter; a maximum offset of 0.46m could be attained. Fig. 4 indicates the 0.45m offset. With respect to coating-thickness variation of high-order functions, the figure indicates that uniformity in height ±2% can be obtained between 0.56 and 0.64m.

In the foregoing discussion, the cover technique was not applied. For uniformity calculations, it was assumed that all vapor sources were small-area sources, obeying the cosine distribution law. Spherical-surface treatment was carried out on the reflective mirror.
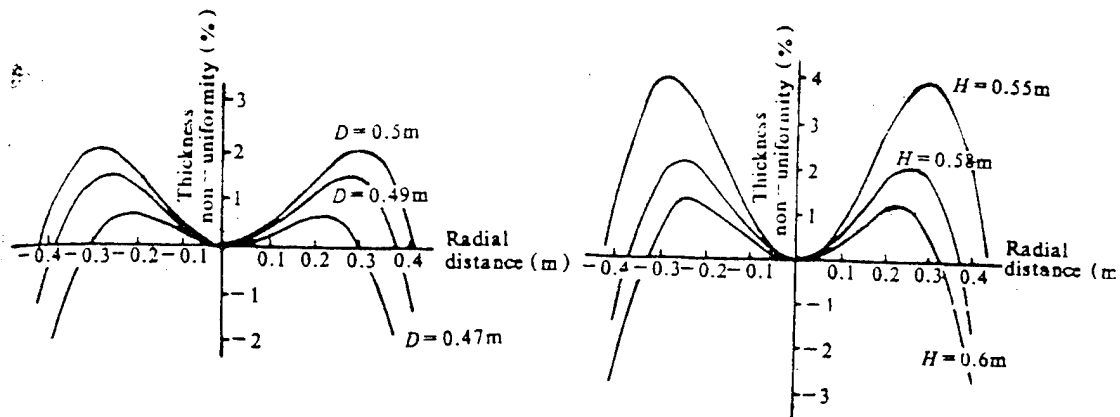
5

Fig.3 Coating thickness non-uniformity for 0.8 meter diameter F/2.0 concave mirror for various offset distance and for a fixed source-to-substrate distance of 0.65 meters.

Fig.4 Coating thickness non-uniformity for 0.8 meter diameter F/2.0 concave mirror distance for various height and a fixed offset distance of 0.45 meters.

III. Initial Design of Coating Thickness

The authors selected the wavelength of the primary laser wavelength in the neighborhood of 1μm; 1.06μm was decided on. The beacon light could be the light diffusely reflected from the target by the primary laser, or a laser at other wavelengths in the relay satellite. The authors employed an artificial beacon light generated by resonance scattering of an 0.5893μm laser by sodium atoms in the alkali-metal layer in meteors in the 80-100km upper atmosphere, as proposed by a French astronomer, Labyrie. It was assumed that reflectivity greater than 99% was required for 1.06μm wavelength; however, reflectivity greater than 95% was required for 0.5893μm wavelength.

6

The initial coating system design was

$$G/Cr/Ag/Al_2O_3/(LH)^2/Air$$

L and H represent, respectively, the SiO_2 and the Ta_2O_5 coating at one-quarter wavelength optical thickness in the primary laser wavelength. Cr and Al_2O_3 were the adherent layers; G was the substrate; and the geometric thickness of Ag was 70nm.

A design was selected that deposited the full one-quarter or half-wavelength medium coating onto the metal; this was chosen because of easy monitoring. The $(LH)^2$ structure was applied in the initial design; this was so because of wider reflectivity at both wavelengths of interest to the researchers. Ag was selected because it has the high-reflectivity L-spectral band, from visible light to infrared. From this design, we can see that the maximum incident angle of the primary reflective mirror was 15°. In the following, a discussion is presented on the polarization properties (ellipticity and phase anomalies) due to nonuniform coating thicknesses with respect to the two wavelengths of interest.

IV. Effect of Thickness Nonuniformity on Ellipticity in the Initial Coating System Design

When linearly polarized light is incident on the primary reflective mirror, other than in the normal direction, the combined reflected light is elliptically polarized light. In other words, there should be a phase difference in the reflected light between the light vector P parallel to the incident surface, and the optical vector S normal to the incident surface. Moreover, there

were different reflective oscillation amplitudes between the two mutually orthogonal components of the two phases. Fig. 5 indicates a functional diagram of coating thickness
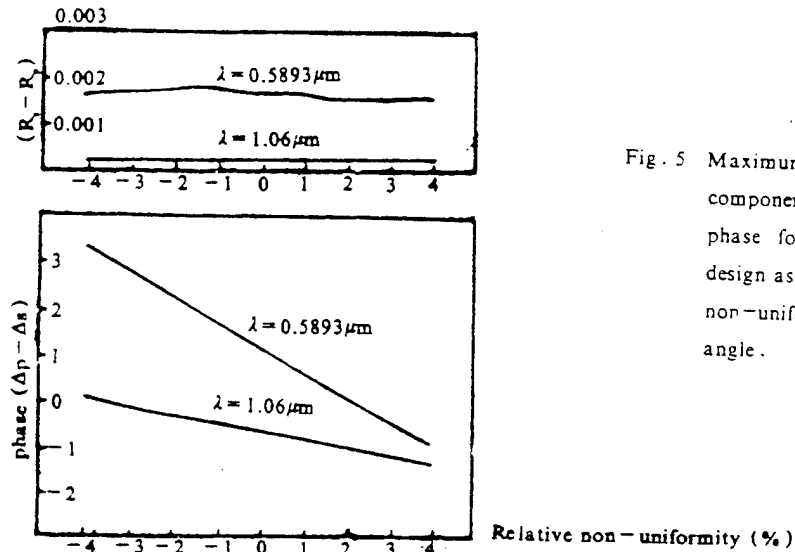

Fig. 5 Maximum difference in p and s components of reflectivity and phase for the initial selected design as a function of thickness non-uniformity for $15°$ incidence angle.

nonuniformity due to variations of refractivity and phase of the primary laser wave and the beacon light wave. At $1.06\mu m$, the phase difference $\Delta p - \Delta s < 1°$. Even when the thickness nonuniformity was 4% and the reflectivity difference in intensity was smaller than 0.02%, the difference in reflectivity was less than 0.02% at $0.5893\mu m$, and the phase difference less than $3.5°$. Generally speaking, there was little effect on ellipticity from the 4% thickness nonuniformity for very oblately polarized light as the reflected light with a $15°$ angle of incidence.

V. Effect of Coating Thickness Nonuniformity on Phase Anomalies at Reflected Waves at Different Wavelengths

8

Nonuniformity in thin-coating properties was exhibited as different optical thicknesses and phase shift differences (phase distortions). The phase shift differences will lead to optical-figure distortions, especially greatly affecting the far-field diffraction properties of the system. Fig. 6 indicates the phase
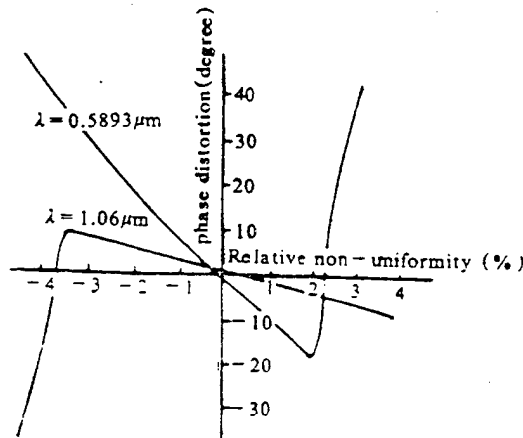

Fig.6 Phase distortion in degrees for the initial selected design at the two wavelengths as a function of thickness non-uniformity for 0.8 meter diameter F/2.0.
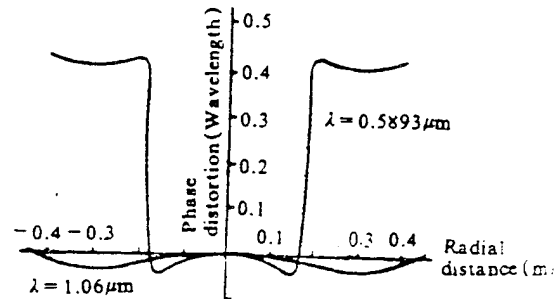
Fig.7 Phase distortion for the initial selected design along the radial distance of 0.8-meter diameter F/2.0 mirror for source-to-substrate height of 0.55 meters and offset distance of 0.45 meters.

distortions in the two reflected waves at the wavelength due to coating-thickness nonuniformity in the initial coating system design. From the figure we can see a -11° or -λ/32.7 wavefront distortion can be generated by +4% nonuniformity at 1.06μm; a phase shift of -2.4° or a wavefront distortion of λ/150 are generated by 1% nonuniformity. The phase distortions were greater at 0.5893μm. The phase shift of 140.28° or a wavefront distortion of λ/257 was generated by 4% nonuniformity. A phase shift of -8.5° or wavefront

9

distortion of $\lambda/42.3$ was generated with 1% nonuniformity.

With respect to a reflective mirror of F/2.0 and 0.8m diameter, Fig. 7 shows the phase distortions of diametral distribution as indicated by wavelength. In the computation, it was assumed that the large mirror surface is approximately spherical; the vapor source-to-substrate distance was 0.55m; and the offset vapor source was 0.45m.

Sign reversal of phase distortions will lead to other problems. Optical-figure errors at a given wavelength can be partially revised with adaptive-optics compensation. If there is sign reversal of wavefront distortions of a light beam at a wavelength, then the wavelength distortions at the wavelength may further degrade the wavefronts at another wavelength during modification. Wavefronts at the two wavelengths should be modified at the same time. The light beams at these two wavelengths applied the same phase distortion signs. Phase distortions of the light beams at both wavelengths should be consistent, if possible. Therefore, another modification design was considered.

VI. Effect on Polarization Properties and Phase distortions in a Modified Design

For the same phase distortion signs, numerous simple designs were studied. Based on theoretical calculations, the modified coating system design was

$$G/\,Al_2O_3/\,Ag/\,Al_2O_3/\,(LH)^2\,\frac{H}{2}\,/\,Air$$

H and L indicate, respectively, the Ta_2O_3 coating and the SiO_2

coating of one-quarter wavelength thickness at the modified

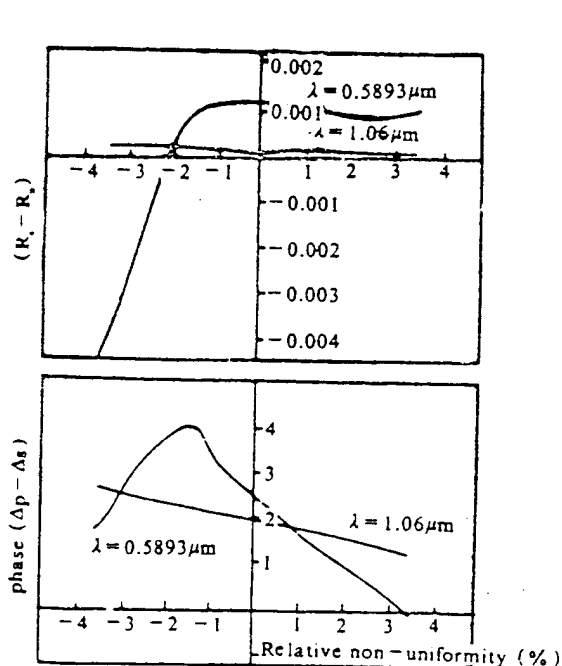wavelength 1.17μm; Al_2O_3 is the adherent layer. Fig. 8 shows

Fig. 8 Maximum difference in *p* and *s* components
of reflectivity and phase for modified design
as a function of thickness non − uniformity
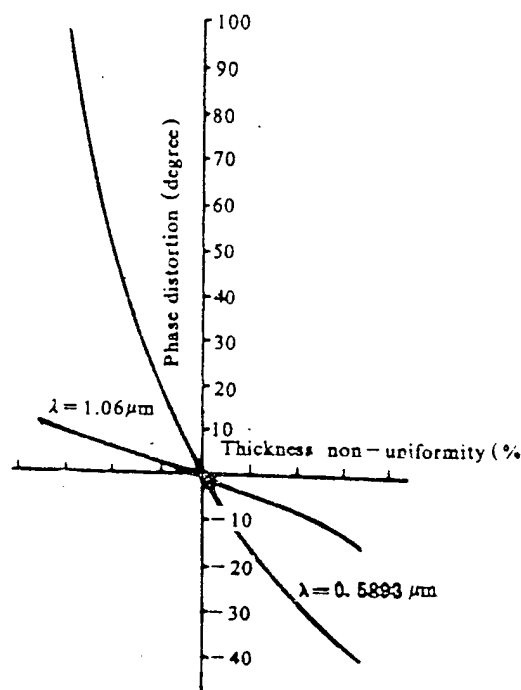for 15° incidence angle.

Fig. 9 Phase distortion in degrees for the modified
design at the two wavelengths as a function
of thickness non − uniformity for 0.8 − meter
diameter *F*/2.0 mirror.

the effect of thin-coating polarization properties due to

nonuniformity in design thicknesses. It was discovered that this

thin coating system design had greater variation with thickness

nonuniformity in reflectivity at 0.5893μm in this coating system

design. Both designs had corresponding reflectivities at 1.07μm.

By comparison with the initial design, the reflectivities at the

11

nonuniformity value of +4% were slightly higher in the modified design; the reflectivity in the modified design at 0.5893μm was lower than in the initial design. In the modified design, Fig. 9 shows the phase distortions generated by two wave beams at different wavelengths due to different nonuniformity. From the figure, we can see that a phase shift of -23° at 1.06μm, or wavefront distortions of λ/15.6 were generated by 4% nonuniformity at 1.06μm; a phase shift of -4.5° or wavefront distortions of λ/80 were generated by 1% nonuniformity. Distortions were greater at 0.5893μm. A phase shift of -55° or wavefront distortion of λ/6.5 were generated at 4% nonuniformity. A phase shift of -14.5° or wavefront distortions of λ/24.8 were generated by 1% nonuniformity. For nonuniformities at different thicknesses, there were the same signs of light beam wavefront distortions at the two wavelengths.
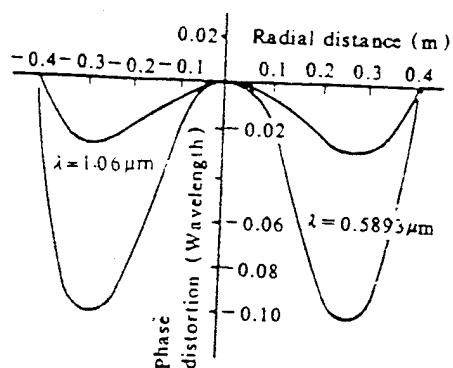

Fig.10 Phase distortion for the modified design along the radial distance of 0.8 – meters diameter F/2.0 mirror for source – to – substrate height 0.56 meters and offset distance of 0.45 meters.

Fig. 10 presents a reflective mirror of F/2.0 and diameter 0.8m; in the modified coating system design, there are phase distortions of the two wave beams along the diametral distribution.

VII. Conclusions

From the foregoing analysis, in the modified coating system design (by depositing optical-thickness-medium coatings of one-quarter or one-eighth wavelengths onto metallic silver), there are the same phase distortion signs generated by light beams at the two wavelengths due to coating thickness nonuniformities. At 15° incidence, there is a smaller effect on polarization in the modified design. It is of interest that the reflectivity was not reduced in the wavelength range. This design was suitable for large mirror surfaces 0.8m in diameter. For easy monitoring, all medium coatings were controlled at the same wavelength. Such same-wavelength monitoring reduced the property changes due to chromatic dispersion of each coating layer under multiple-wavelength control.

The first draft of the article was received on July 23, 1991; the final, revised draft was received for publication on September 20, 1991.

REFERENCES

2. Tang Jinfa and Gu Peifu, <u>Bomo Guangxue Yu Jishu</u> [Thin-Film Optics and Technology], Mechanical Engineering Publishing House, 1989.

EFFECT OF PHASING ERRORS ON BEAM COMBINATION

Hu Zhiping, Le Shixiao, Song Ruhua, and
Zhou Hongyang

Hu, Le and Song of University of Electronic Science and Technology,
Chengdu 610054; Zhou of China Academy of Engineering Physics, P.O.
Box 532, Chengdu 610003

BSTRACT Based on the research beam control for synthetic aperture systems in free space. this paper analyzes and discusses effects of phasing errors on beams combination. The phasing errors include piston errors, tilt errors and focus errors. The corresponding physical models are developed . Finally results of numerical computations are given.

EY WORDS synthetic aperture systems, beam control, beams combination, piston errors, tilt errors.

I. Introduction

For a synthetic-aperture system as a single coherent high-power laser emission system, in recent years the system was of growing concern to researchers. By controlling the wavefront phases of beams (emitted at various subapertures) of a synthetic-aperture system, coherent far field combination of light beams can be carried out. However, when controlling the wavefront phases of the emitted light beams, generally there will be errors in phase control with various factors affecting phase control, leading to degraded properties of the synthetic-aperture system and reducing

the peak-value light intensity coherently combined in the far field. The authors developed studies on the concept of light beam control of the synthetic-aperture system in the ideal situation without considering various factors affecting precision phase control of the light beams. Thus, a physical model for coherent and noncoherent combination of light beams, as well as beam-pointing and beam-shifting were are presented. Theoretical analysis and numerical simulation calculations were conducted [2,3]. On the basis of the developed work, the article further analyzes and discusses the factors affecting precise control of light beam phases (piston and tilt errors of tuned phase, and tuned-focus errors), and the effects on coherent combination of light beams. In addition, numerical simulation calculations and three-dimensional diagrammatic demonstrations were conducted.

II. Theoretical Analysis and Numerical Simulation Calculations

For the theoretical analysis, the authors assumed that the light beams emitted from the emission system of a laser device are plane-wave laser beams:

$$U_0(x_1, y_1) = B p_l(x_1, y_1) \tag{1}$$

In the equation, B is a constant. For convenience in the following analysis, we set B=1; $p_1(x_1, y_1)$ is the pupil function of the emission system, with the following definition:

$$p_l(x_1, y_1) = \begin{cases} 1 & x_1^2 + y_1^2 \leqslant (d/2)^2 \\ 0 & (x_1^2 + y_1^2) > (d/2)^2 \end{cases} \tag{2}$$

In the equations, d is the pupillary diameter.

15

Assume that the synthetic-aperture system is composed of N=lxm subapertures. For each subaperture, its center coordinates are $x_t(i,j)$, $y_t(i,j)$,i=1,2,...,1; j=1,2,...,m. The combined light field at the far field target is[2]:

$$U(x,y) = A(x,y,z)F\{\sum_{i=1}^{l}\sum_{j=1}^{m}p_l(r_{i,j})\}|_{\substack{(x-x_i)/\lambda z \\ (y-y_i)/\lambda z}}$$

$$= A(x,y,z)F\{p_l(r_1)\}|_{\substack{(x-x_i)/\lambda z \\ (y-y_i)/\lambda z}}$$

$$\cdot \sum_{i=1}^{l}\sum_{j=1}^{m}\exp\{-2\pi j[\frac{x-x_i}{\lambda z}x_i(i,j)+\frac{y-y_i}{\lambda z}y_i(i,j)]\}$$

In the equations, A(x,y,z)=exp[(jkz)·exp((jk/2z)(x²+y²)]/(jλz), F{ } represents the Fourier transform. k=2π/λ, λ is wavelength, and (x_t, y_t) are the coordinates of the pointing dot. Let $x_t=y_t=0$ (the light beams emitted from various subapertures converge onto the axial line), then we obtain

$$U(x,y) = A(x,y,z)F\{p_l(r_1)\}|_{\substack{x/\lambda z \\ y/\lambda z}}$$

$$\cdot \sum_{i=1}^{l}\sum_{j=1}^{m}\exp\{-2\pi j[\frac{x}{\lambda z}x_i(i,j)+\frac{y}{\lambda z}y_i(i,j)]\} \qquad (3)$$

Obviously, from Eq. (3) we know that the peak-value light intensity in coherent combination is

$$I_M = |U(0,0)|^2 = \frac{1}{\lambda^2 z^2}|F\{p_l(r_1)\}|^2\cdot(l\times m)^2 = N^2\cdot I_{1M} \qquad (4)$$

In the equation, I_{1M} indicates the peak-value light intensity of a single subaperture system at (0,0,z).

16

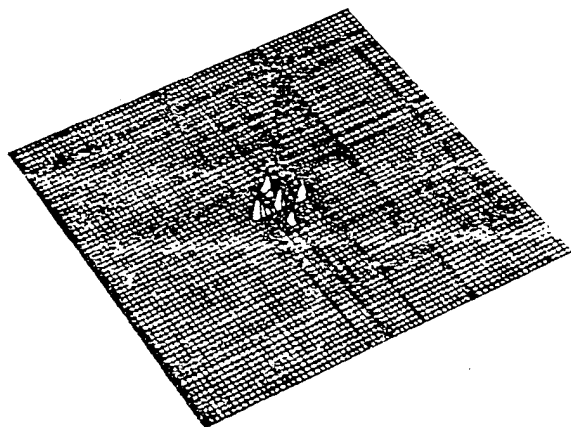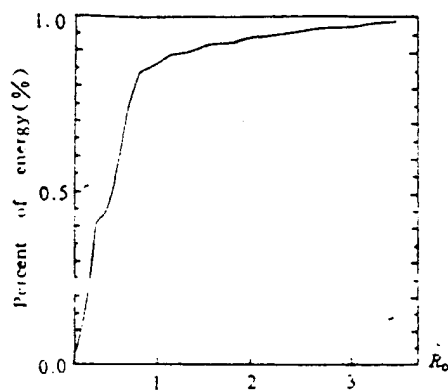In the following analysis and calculations, we let N=16, d=1m, λ=1μm, and z=10^3km.

Fig. 1 The intensity distribution of coherent beams combination

E (AIRY DICS)/ E(TOTAL) = 86.8 %

Fig. 2 The regional energy distribution in the far−field. E = 86.8%

Fig. 1 shows the light-intensity distribution of beams coherently combined in the synthetic-aperture system; the data in the figure indicate the relative values of peak-light intensities, which are the same as later on. Fig. 2 shows the regional energy distribution curve of light beams coherently combined in the far field. In the figure, R_D indicates the radius of the Airy disc. E(AIRY DISC)/E(TOTAL)=0.868299E+00 indicates that the percentage of energy in the first Airy disc is 86.8299% of the total energy. R_D=0.61 x λ x z/b; the unit is 0.61 x λ z/b. λ is wavelength; z is the mirror-to-target distance; and b is the equivalent pupillary radius of the phase control array.

1. Effect of piston errors [4] of the tuned phase

The piston errors of the tuned phase stem from the phase-error term when tuning and controlling the wavefront phase of the light beams emitted from the subapertures, such as $\exp(jk\phi_{ij})$ (ϕ_{ij} is not related to x_1, y_1). Therefore, the light field distribution coherently combined in the far field varies as:

$$U_p(x,y) = A(x,y,z) F\{p_1(r_1)\}\Big|_{y/\lambda z}^{x/\lambda z}$$

$$\cdot \sum_{i=1}^{l}\sum_{j=1}^{m} \exp\left[-2\pi j\left(\frac{x}{\lambda z} x_1(i,j) + \frac{y}{\lambda z} y_1(i,j)\right)\right] \cdot \exp(jk\varphi_{ij}) \qquad (5)$$

Thus, the coherently combined peak-value light intensities become

$$I_{Mp} = |U_p(0,0)|^2$$

$$= \frac{1}{\lambda^2 z^2}\left|F\{p_1(r_1)\}\Big|_0^0\right|^2 \cdot \left|\sum_{i=1}^{l}\sum_{j=1}^{m} \exp(jk\varphi_{ij})\right|^2 \qquad (6)$$

Generally, there is $\left|\sum_{i=1}^{l}\sum_{j=1}^{m}\exp(jk\varphi_{ij})\right|^2 \leqslant N^2$. Therefore,

$$I_{Mp} \leqslant N^2 \cdot I_{1M}$$

In other words, the piston errors of the tuned-phase light beams will lead to a decrease in peak-value light intensity.

Figs. 3 and 4 are, respectively, the light-intensity distribution diagram and the regional energy distribution curve of the far-field combination light beams under the situation of $\phi_{ij}=0$ with respect to $\phi_11=\phi_12=\phi22=0.5\lambda$. From these figures, we can see
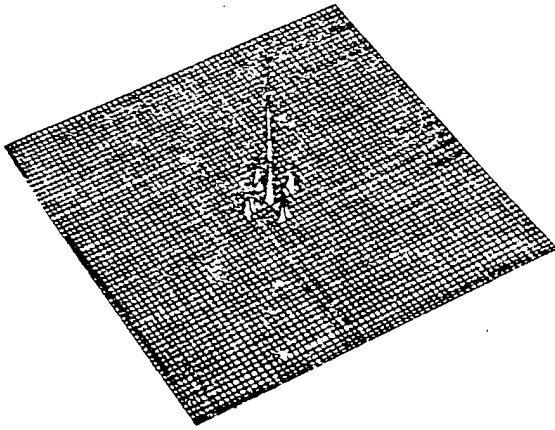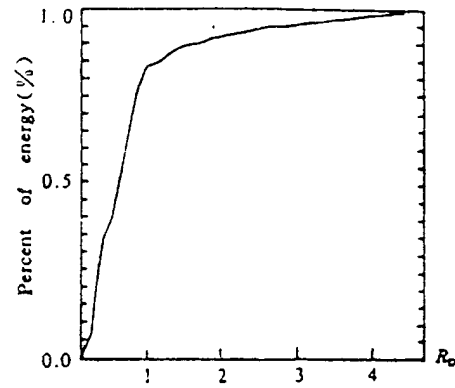
18

E (AIRY DICS) / E(TOTAL) = 86.5 %

Fig. 4 The regional energy distribution in the far field with the piston errors. ($\varphi_{11} = \varphi_{12} = \varphi_{21} = \varphi_{22}$ = 0.5λ , other ϖ_{ij} = 0). E = 86.5%

Fig. 3 The intensity distribution with the piston errors. ($\varphi_{11} = \varphi_{12} = \varphi_{21} = \varphi_{22}$ = 0.5λ , other φ_{ij} = 0)

that the piston errors in the tuned phase will lead to decreased peak-value light intensities with light beam combination; however, the effect is smaller on energy percentage in the first Airy disc.

2. Effect of tilt errors of tuned phase [4]

Tilt errors of the tuned phase signify the phase-error term due to tilt and wobbling of the subapertures in bringing forward such as $\exp\{[jk[c_{ijx}(x-x_s(i,j))+c_{ijy}(y-y_s(i,j))]\}$ when controlling the wavefront phase of the light beams emitted from the subapertures. Here, the combined light-field equation of the light beam should be

$$U_{\tau}(x,y) = A(x,y,z)\sum_{i=1}^{i}\sum_{j=1}^{m} F\{ p_i(r_{ij}) \cdot \exp[jkc_{ijx}(x_i-x_j)+jkc_{ijy}(y_i-y_i)]\}\Big|_{y/\lambda z}^{x/\lambda z}$$

$$= A(x,y,z)\sum_{i=1}^{i}\sum_{j=1}^{m} F\{ p_i(r_i)\exp[jk(c_{ijx}x_i+c_{ijy}y_i)]\}\Big|_{y/\lambda z}^{x/\lambda z}$$

$$\cdot \exp[-2\pi j(\frac{x}{\lambda z} x_s + \frac{y}{\lambda z} y_s)]$$

$$= A(x,y,z) \sum_{i=1}^{l} \sum_{j=1}^{m} F\{p_l(r_1)\}|_{(x-c_{ij}z)/\lambda z}^{(x-c_{ij}z)/\lambda z}$$

$$\cdot \exp[-2\pi j(\frac{x}{\lambda z} x_s(i,j) + \frac{y}{\lambda z} y_s(i,j))] \qquad (7)$$

Obviously, here the peak-value light intensity becomes

$$I_{MT} = |U_T(0,0)|^2$$

$$= \frac{1}{\lambda^2 z^2} |\sum_{i=1}^{l} \sum_{j=1}^{m} F\{p_l(r_1)\}|_{-c_{ij}/\lambda}^{-c_{ij}/\lambda}|^2 \leqslant \frac{1}{\lambda^2 z^2} |\sum_{i=1}^{l} \sum_{j=1}^{m} F\{p_l(r_1)\}|_{0}^{0}|^2 = N^2 I_{1M} \qquad (8)$$

Figs. 5 and 6 are, respectively, the light-intensity distribution diagram and the regional energy distribution curve of light beams combined when $c_{ijx}=c_{ijy}=0.5 \times 10^{-6}$ rad. From the above-mentioned diagrams and curves we know that the tilt errors of the tuned phase not only reduce the peak-value light intensity of the far field beam combination, but also lead to energy reduction in the first Airy disc. The greater the tilt errors in the tuned phase, the more pronounced is such effect.

3. Effect of light beam tuning focus error

When focussing the light beams, if the light beams are not accurately converged, the following phase term of focus errors [2] will be generated:

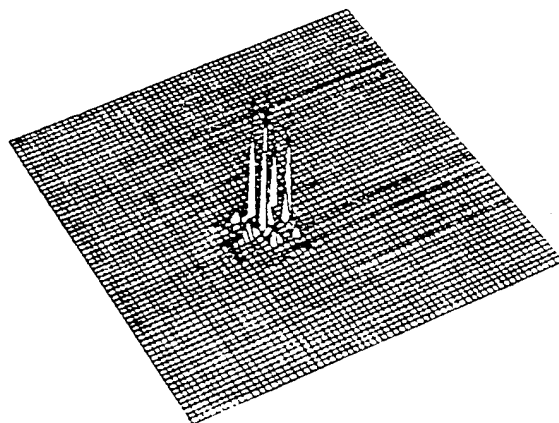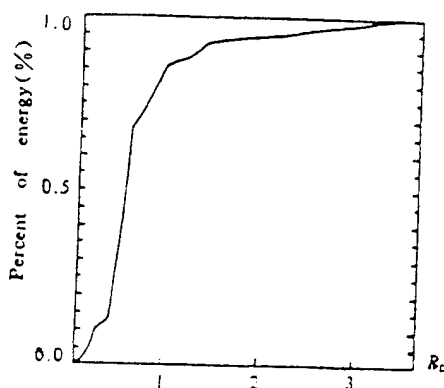$$\exp\{jk\varepsilon_{ij}[(x_s-x_s(i,j))^2+(y_s-y_s(i,j))^2]/2\}$$

E AIRY DICS E TOTAL $= 85.6$ %

Fig. 5 The intensity distribution with the tilt errors. ($c_{ijx}=c_{ijy}=0.5 \times 10^{-6}$ rad)

Fig. 6 The regional energy distribution in the far field with the tilt errors $c_{ijx}=c_{ijy}=0.5 \times 10^{-6}$ rad) $E = 85.6$%

Thus, there is the light field in the far-field beam combination:

$$U'_F(x,y) = A(x,y,z) \sum_{i=1}^{l} \sum_{j=1}^{m} F\{p_i(r_{1ij}) \cdot \exp[jk\varepsilon_{ij}((x_1-x_i)^2+(y_1-y_i)^2)/2]\}\Big|_{y/\lambda z}^{x/\lambda z}$$

$$= A(x,y,z) \sum_{i=1}^{l} \sum_{j=1}^{m} F\{p_i(r_1)\exp(jk\varepsilon_{ij}r_1^2/2)\}\Big|_{y/\lambda z}^{x/\lambda z}$$

$$\cdot \exp\{-2\pi j[\frac{x}{\lambda z} x_i(i,j) + \frac{y}{\lambda z} y_i(i,j)]\}$$

Let $\varepsilon_{ij}=\Delta_{ij}/z$, then we have

$$U_F(x,y) = A(x,y,z) \sum_{i=1}^{l} \sum_{j=1}^{m} \{p_i(r_1)\exp(jk\Delta_{ij}r_1^2/2z)\}\Big|_{y/\lambda z}^{x/\lambda z}$$

$$\cdot \exp\{-2\pi j[\frac{x}{\lambda z} x_i(i,j) + \frac{y}{\lambda z} y_i(i,j)]\} \tag{9}$$

Therefore, the peak-value light intensity of the beam

26

combination is:

$$I_{MF} = \left| U_F(0,0) \right|^2 = \frac{1}{\lambda^2 z^2} \left| \sum_{i=1}^{l} \sum_{j=1}^{m} F\{ p_i(r_i) \exp(j\pi\Delta_{ij} r_{ij}^2/\lambda z) \} \Big|_0^0 \right|^2$$

$$\leqslant \frac{1}{\lambda^2 z^2} \left| \sum_{i=1}^{l} \sum_{j=1}^{m} F\{ p_i(r_i) \} \Big|_0^0 \right|^2 = N^2 I_{1M} \tag{10}$$

Fig. 7 is the light intensity distribution diagram at $z=5\times10^4$m of a light-beam coherently combined when there are no focus errors. Fig. 8 is the light intensity distribution diagram while the beam combination at $z=5\times10^4$m when there are focus errors (that is, when $\Delta_{11}=\Delta_{12}=\Delta_{21}=\Delta_{22}=\Delta_{31}=\Delta_{32}=\Delta_{41}=\Delta_{42}=0.1$ and $\Delta_{13}=\Delta_{14}=\Delta_{23}=\Delta_{24}=\Delta_{33}=\Delta_{34}=\Delta_{43}=\Delta44=-0.1$; in the physical significance, in some of the subapertures, the light beams are focussed ahead of the common pointing dot, and the remaining subapertures have the beams focussed behind the common pointing dot. Obviously, we know that the peak-value light intensities here are apparently reduced; the greater the focus errors, the more pronounced is the effect on the beam combination.

III. Conclusions

In the foregoing, detailed analysis and discussion were given concerning the factors affecting precision control of light beam phases in the synthetic-aperture system; moreover, numerical simulation calculations were conducted. As shown in the calculation results, since precision control of the light
beam phases cannot be carried out, this will lead to a situation in which the peak-value light intensities of the beam combination are
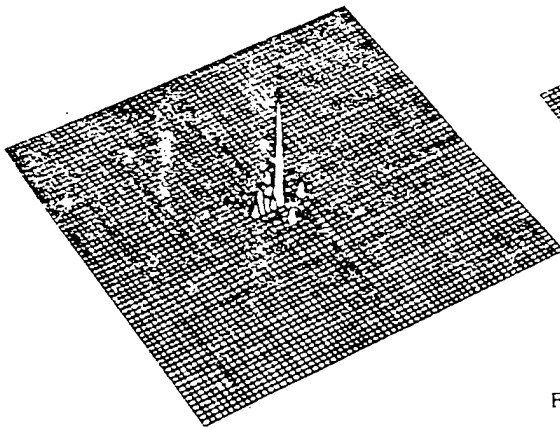
Fig.7 The intensity distribution of coherent beams combination without focus errors. $(\Delta_{ii}=0)$, $z=5\times10^4$ m.
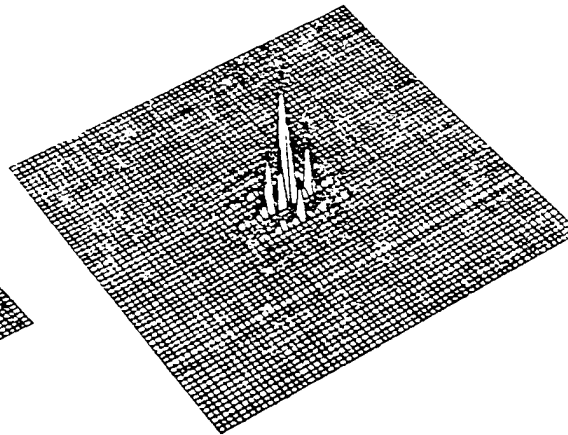
Fig.8 The intensity distribution with the focus errors. $(\Delta_{11}=\Delta_{12}=\Delta_{21}=\Delta_{22}=\Delta_{31}=\Delta_{32}=\Delta_{41}$, $\Delta_{42}=0.1$, $\Delta_{13}=\Delta_{14}=\Delta_{23}=\Delta_{24}=\Delta_{33}=\Delta_{34}=\Delta_{43}$, $=\Delta_{44}=-0.1)$, $z=5\times10^4$ m.

reduced. However, we have to point out that the factors affecting the light-beam phase control are assumed to be static variables, not random and dynamic variables in the above-mentioned analysis and discussion. However, with respect to laser propagation in the atmosphere, of more practical significance is a discussion of the effect of beam-phase precision control by such random and dynamic variables of atmospheric turbulence. In later work, we will gradually develop research on this aspect in order to obtain physical models affecting light beam phase control that more practically match the situation in atmospheric turbulence.

23

the institute.

REFERENCES

2. Hu Zhiping et al., "Physical model and computer simulation demonstration controlled by planar-wave light beam," Dianzi Keji Daxue Xuebao [Bulletin of University of Electronics Science and Technology], 18(5), 462 (1969).

5. J. W. Goodman, On Fourier Optics, Chapters 6 and 7, Science Publishing House, Beijing, 1979

EXPERIMENTAL RESEARCH ON THERMAL BLOOMING EFFECT INDUCED BY HIGH POWER LASER PULSES

Wu Yi, Wang Yingjian, Wang Chao, and Hou Zaihong

Anhui Institute of Optics and Fine Mechanics
P.O. Box 25
Hefei 230031

ABSTRACT Experiments on the establishing and vanishing time features of thermal lens in the moving or static absorbing cell, the beam diverging features at far field through the blooming cell, the comparision of the beam distortion features of nonuniform absorption with that of uniform absorption are reported.

KEY WORDS propagation, absorption, thermal, blooming.

I. Introduction

When a high power laser beam propagates through the atmosphere, air along the beam path is heated since the gases absorb laser energy, thus inducing the thermal blooming effect of the laser beam. Research on the thermal blooming effect during the atmospheric propagation of high power laser beams was conducted for many years [1,2]. In the authors' research problems, a laser beam will be propagated upward to a height of about 1000km. The atmospheric layers are thinner compared to

25

this 1000-km of propagation through the absorption medium. In addition to the bulk absorption coefficient directly inducing the thermal blooming effect, there is also the effect of the atmospheric wind field (including light beam rotation). After the laser beam is subjected to the thermal blooming effect when passing through the absorptive atmospheric layers, the beam continues to propagate for a long distance in a vacuum. The variable features of the beam are the subject of interest to the authors. In addition, the nonuniformity of atmospheric absorption was theoretically analyzed in [3] as regards the upward propagation thermal blooming effect for high power lasers. As indicated in the analytical results, there are obvious differences between uniform absorption and nonuniform absorption with respect to the thermal blooming effect. In other words, the traditional concept of considering the atmosphere as consisting of homogeneous absorptive layers is not at all appropriate.

Based on these considerations, the article reports on simulation experiments that the authors conducted in their laboratories: (1) under the simulated conditions of windy and static absorbing gases, studies were conducted on the time features of the formation and disappearance of monopulse laser thermal lenses. (2) Under conditions of uniform and nonuniform absorption (the total absorption coefficients of the two kinds are kept equal), studies were conducted on the differences in thermal blooming of a laser beam. (3) After generation of a thermal lens, a study was made on the distortion divergence

properties of a laser beam over a longer distance other than in an absorptive medium. The theoretical calculations in the article are based on the geometric-optics method described in [1].

II. Experimental Conditions and Parameters

Fig. 1 shows the entire setup of the experimental system. The primary laser was a TEACO$_2$ monopulse laser. By using the P-Ge pulling device, variations of the central light intensity were detected. A model 7623A100M storage [illegible] oscilloscope was used in recording. He-Ne light and a CO$_2$ laser beam were passed coaxially through a simulation absorption channel; a CCD detection system was used to monitor the light beam distortion process. A four-section structure simulation absorption channel was employed, capable of passing through two light beam channels. One pass (OD=30mm) served to propagate the high power laser beam. Another pass (OD=25mm) was used to monitor the absorption coefficient in the various sections of the channel with a bomb calorimeter for light splitting (into faint light) in the light pass. Propane was used as the absorption gas. This gas was fed while controlling the amount absorbed during the various passes; then air was admitted until 1.01x10^{5}Pa was reached. In the figure, the concave reflective mirrors R$_1$ and R$_2$ tuned the 10.6μm laser beam into a nearly aligned light beam to pass through the simulated absorption path. The light-spot radius at the 1/e power level was 5mm. The parallel light
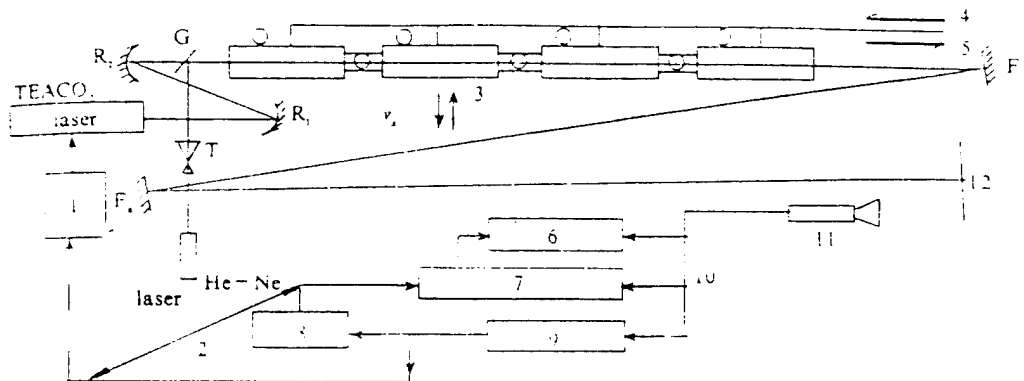
Fig. 1   Thermal blooming simulation system (v₁ motion)

1. synchronous laser power   2. synchronous signal   3. simulated absorption system
4. gas out   5. gas fill   6. monitor   7. computer sample system   8. PC interface
9. synchronous control   10. video signal   11.CCD camera   12. view screen

tube T tuned the He-Ne light to a slightly divergent light beam
which was passed through a germanium lens G to be tuned to the
same axis as the CO_2 laser. The reflective mirror F_n reflected
the He-Ne light several times in the laboratory in order to
obtain the intensity distribution after passing through the
medium for the light beam in far field propagation (the longest
distance was z=30m). With the measurements, the authors obtained
the following experimental parameters:

(1) TEACO₂ energy E=0.55J, and pulse duration $\tau_p = 20\mu s$

(2) overall absorption coefficient $\alpha_t = 0.193/m$

(3) section-by-section nonuniform absorption coefficient

$\alpha_1 = 0.4825/m, \ \alpha_2 = 0.2413/m, \ \alpha_3 = 0.0483/m, \ \alpha_4 = 0$,

satisfying (L/4) $\sum_i \alpha_i = \alpha_t L$

(4) length of absorption pass, L=4.6m

28

(5) thermal distortion parameter $N = -2\mu_t E\alpha_t L^2 \pi \rho c_p a^4 = 1.65$

in the parameters $\rho = 1.2 \times 10^{-3} g/cm^3$ (gas density)

$c_p = 1 J/g \cdot K$ (constant-pressure specific heat of the gas

$\mu_t = -9.5 \times 10^{-7} K^{-1}$ (dn/dT, derivative of refractivity with respect to temperature)

$a_{CO2} = 5mm$ (light spot at $1/e$ power level)

(6) for the He-Ne light emitted beam, the light-spot radius $a_0 = 8.84mm$ (at channel exit)

$a(z=30) = 10.35mm$ (30 mm from channel exit)

(7) for He-Ne light, the Fresnel number $F(30m) = 1.64$ (basically satisfying the far field conditions).

The real-time synchronous quantized CCD detection system consists of a CCD-camera, a video frequency screen, and a computer. In the central portion, the main indicators of the CA53 video frequency monitor were the range of the 8-bit dynamic A/D, and D/A; the real-time four-frame 512x512 memory and 25-frames-per-second acquisition speed. In addition, through a 74LS123, two-channel triggering was conducted, thus obtaining the synchronous triggering of the video frequency field, and the time-division delay triggering pulses with 40ns as the full cycle in order to carry out synchronization between the CCD-camera and the monopulse laser device, as well as the acquisition of light-spot information at various time instants.

III. Data Acquisition and Treatment Method

Due to the restriction on the dynamic range (8 bits) of the

acquisition board, consideration was given to repeatability of the thermal blooming effect. In precision synchronous control, the authors applied instant-by-instant light exposure method to obtain the nonsaturated A/D conversion signal. Fig. 2 shows the one-dimensional intensity curve of the original He-Ne light
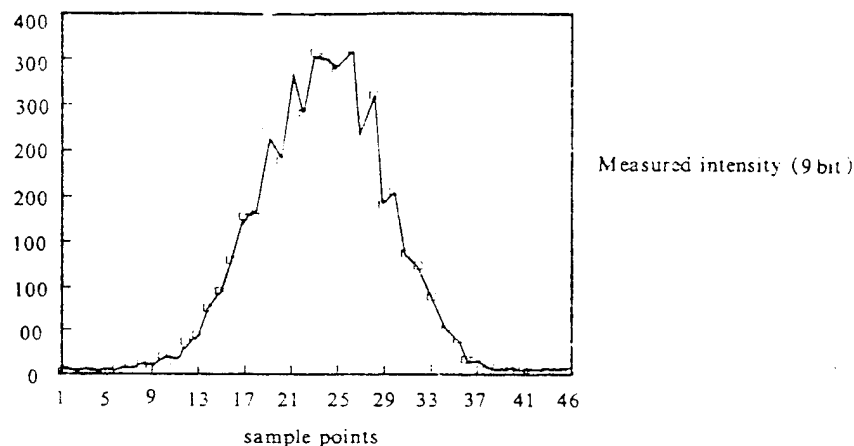

Measured intensity (9 bit)

sample points

Fig.2 Original intensity of He−Ne laser (1D)

intensity. By using two light exposure times of 1/250s (ρ_1 light intensity) and 1/500s (ρ_2 light intensity), the authors obtained:

$$\rho_0 = \begin{cases} A\rho_2 - 255 & \rho_2 \geqslant 255/A \\ 0 & \rho_2 < 255/A \end{cases} \tag{1}$$

In the equation, A=500/250=2, ρ_0 is the portion of saturated intensity to ρ_1. However, the actually collected light intensity $\rho=\rho_1+\rho_0$. Thus, the measured A/D conversions reached the maxiµm value of 512 (9 bits). At the various time instants, the errors of the light-spot intensity $E=\int \rho\,ds$ does not exceed 5%.

Calculation of light-spot radius:

$$<r^2> = \int |r - r_c|^2 \rho\, ds \Big/ \int \rho\, ds \tag{2}$$

In the equation, r_c is the position of the light-spot center of gravity; ds=dxdy, $r_c=(x^2_c+y^2_c)^{1/2}$; however

$$ds = dx\,dy,\; r_c = (x_c^2 + y_c^2)^{1/2} \text{ 而 } x_c = \int x\rho\, ds \Big/ \int \rho\, ds;\; y_c = \int y\rho\, ds \Big/ \int \rho\, ds.$$

With respect to the results of the secondary light exposure, Eq. (2) can be processed into:

$$<r^2> = \frac{\int |r - r_c|^2 \rho_1\, ds + \int |r - r_c|^2 \rho_0\, ds}{\int \rho_1\, ds + \int \rho_0\, ds} \tag{3}$$

Let

$$E_1 = \int \rho_1\, ds;\; E_0 = \int \rho_0\, ds;\; <r_1^2> = \int |r - r_c|^2 \rho_1\, ds / E_1;\; <r_0^2> = \int |r - r_c|^2 \rho_0\, ds / E_0$$

We obtain:

$$<r^2> = \frac{<r_1^2> + <r_0^2> E_0/E_1}{1 + E_0/E_1} \tag{4}$$

With the energy statistics of the light-spot radii, we can calculate that the light beam divergence angle is

$$<\theta> = \Delta<r> / \Delta z \tag{5}$$

In the equation, $\Delta<r>$ is the difference between two points of the light-spot radius in the propagation distance; Δz is the difference of the distance between two points.

IV. Experimental Results and Discussion

Fig. 3 shows the variation of laser beam intensity with time at the center and after distortion of the CO_2 laser beam. From Fig. 3 (b), we can clearly see the obvious nonlinear attenuation
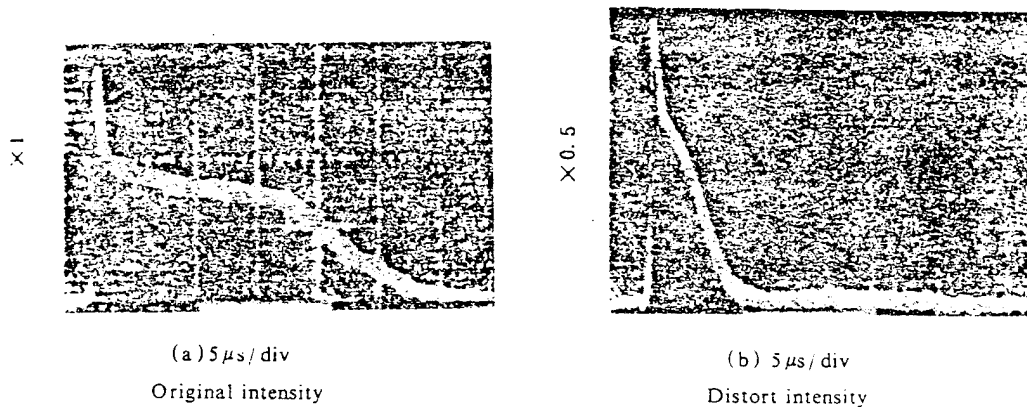

(a) $5 \mu s / $div
Original intensity

(b) $5 \mu s /$ div
Distort intensity

Fig.3 Curves of CO_2 laser intensity at centre point

effect due to thermal blooming. In other words, at the most crucial instant, t=7.5μs of thermal distortion, the light-spot center intensity is nearly zero. This results from expanding the light beam with the thermal lens. Besides, based on the linear attenuation difference for the 10.6μm laser due to the absorption gas, from Fig. 3 we can see that the time t=5μs when the thermal lens begins to form.

Fig. 4 shows the variation of the thermal blooming light spots at various instants when the absorption channel is quiet, and after the action of the CO_2 laser by the coaxial He-Ne light, due to the thermal lens effect. At t=0, this indicates the instant of CO_2 laser action. We can see that in the early period

After pulse $t = 40$ms $t = 80$ms   Original

(a) Blooming patterns of He−Ne laser

(a) He−Ne 光畸变光斑

a: $t =$ After pulse
b: $t = 20$ms
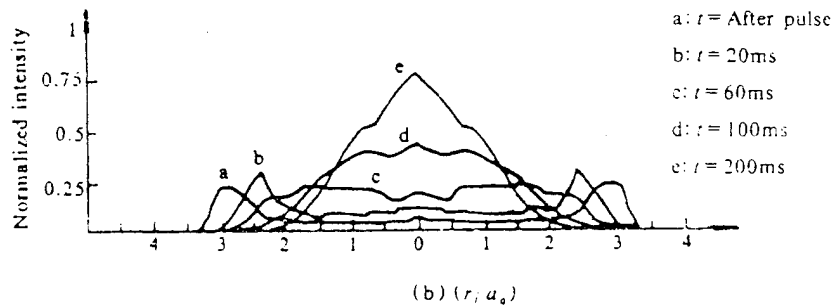c: $t = 60$ms
d: $t = 100$ms
e: $t = 200$ms

(b) ($r_i a_0$)

Fig. 4   Blooming intensity (1D) of He−Ne laser at different time

of laser action (t<20ms), the He-Ne light undergoes a considerable expansion. The light-spot energy radius is three times the radius of the original light spot at the 1/e power level. This result is quite different from the authors' theoretical calculations [5]. However, in the later period (t>40ms) of the thermal lens, the experimental results and the theoretical calculated results are relatively close to each other (refer to Fig. 5). This indicates that the later period of the thermal lens has the thermal propagation playing a major role. Under such conditions, complete restoration of the light spot requires more than 20ms.

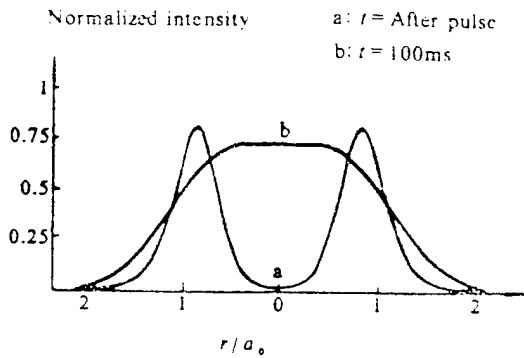Fig. 6 shows the measured He-Ne light when the absorption

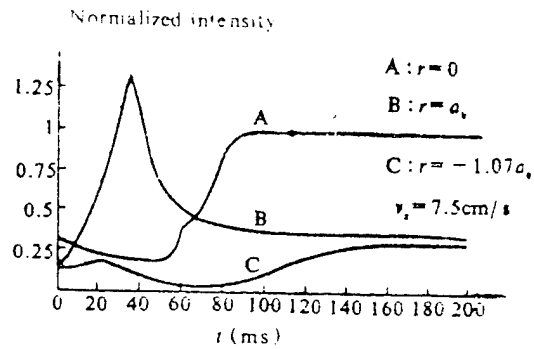Fig.5 Curves calculated on blooming intensity
(1D) of He-Ne laser

Fig.6 Time-variation curves measured at 3-points
in the condition of simulated wind

channel moves with respect to the time-based variation (near-field) of light intensity at three points of the windward direction radius. Curve A is the light-spot center; B is the windward point r=a beginning from the center; c shows the reverse direction r=-1.076a. From the figure, we can see that the restoration time of point A is 90ms. In the distortion process of point B, due to the effect of the wind, the light intensity exceeds the original value of light intensity at the center at approximately 40ms. The restoration time is 150ms. The foregoing results explain that the atmospheric wind field has a certain function in smoothing out the thermal lens effect. However, it simultaneously brings with it the problem of deviation of the light-beam center intensity.

In the theoretical-calculation model, both the CO_2 laser and the He-Ne laser applied the ideal limited gaussian light beams. However, in the experiments the light-spot intensity distributions of the CO_2 and the He-Ne lasers showed certain fluctuations, see Fig. 2 and [4]. With respect to the results of

the experiments and the theoretical calculations, there are
obvious differences when t is less than tens of milliseconds.
The authors analyzed that this is due to the following reasons
[5]: (1) nonuniformity of the CO_2 intensity distribution leads to
fluctuations in refractivity variation in the propagation path,
thus not only leading to enhancement of thermal scattering of
light intensity in the small scale nonuniformity of the CO_2
laser, but also enhancing the nonuniform light intensity in the
small dimensions of the He-Ne light. Thus, the scattered energy
to a greater angle is greater than the calculation results of
using the homogeneous gaussian model. In other words, the
observed light beam expansion is greater than the thermal
blooming expansion of the light beam without perturbation. (2)
Since there are fluctuations in intensity and phase for the He-Ne
laser beam, under the action of the coaxial high power laser,
light beam distortion is more serious than distortion of the
He-Ne laser beam in the absence of perturbation of the entire
beam; the expansion is also greater. In short, the experimental
results of the light beam expansion are apparently greater than
the theoretical calculation results, for the following reasons:
small-dimension light intensity and phase perturbation bring
about instability of thermal blooming. However, over a longer
time period after the action of the pulsed laser, the thermal
lens tends to smooth out, and the effect of small-dimension
nonuniformity is reduced. The results of the experimental and
theoretical calculations of light beam thermal blooming in the

absence of perturbation tend to be consistent.

As shown in Fig. 7, after the action of the monopulse CO_2 laser, the light-spot radius of the near-field distortion of the
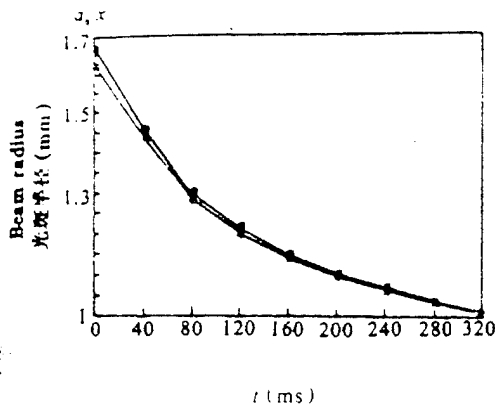

Fig.7 Comparison of Blooming radius due to
      nonuniform absorption to that due to
      uniform absorption
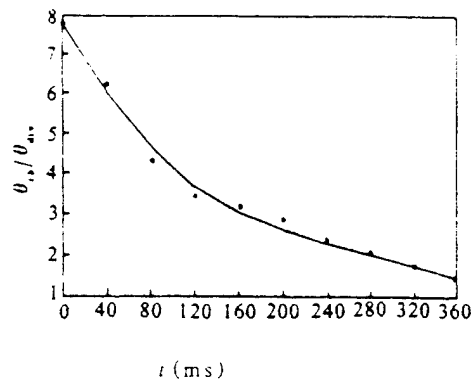   □ nonuniform absorption — uniform absorption

Fig.8 Time—variation of relative spreading—angle
      of He—Ne beam in the far—field

coaxial He-Ne light beam varies with time. The upper and lower curves indicate, respectively, the results of nonuniform and uniform absorption conditions. In the experiments, it is maintained that the overall absorption rate $\int \alpha(z)dz = \alpha_t$, with L remaining constant in both situations. We can see that time periods for the formation and disappearance of the thermal lens are consistent in time. However, the thermal distortion light-spot radius under nonuniform absorption conditions is apparently larger than the thermal-blooming light-spot radius in the case of uniform absorption. At the beginning, the difference between the two cases was 0.4mm. In other words, in the case of nonuniform

36

absorption conditions, the divergence angle of the thermal-blooming light beam is greater than the divergence angle of thermal-blooming light beam under uniform conditions, by about 3%. This is due to the integration relationship of thermal distortion parameter N and $\int_0^L (L-z)\alpha(z)\exp[-\tau(z)z]dz$. Since the propagation direction of the light beam is from high to weak absorption, in the front end of the simulation channel, parameter N is greater in the nonuniform absorption situation, and its lens effect is also greater. However, propagation to the rear end, since the reduced absorption of laser energy and the reduction in energy distribution density due to distortion, the effect of parameter N is weakened. Thus, we can say, upon considering the problem of upward propagation of a high power laser through the atmosphere, it is inappropriate to consider the effect of thermal blooming with the equivalent uniform absorption model. In addition, due to the reverse directions of upward and downward propagation, the thermal blooming effect is irreversible with respect to the nonuniform absorbing atmosphere.

Another problem we examined was that, relatively speaking, the atmospheric layers are very weak for upward laser propagation to approximately 1000km. With respect to the problem of very weak absorption layers, how the generated thermal blooming affects the far field propagation of a laser beam in a vacuum? Fig. 8 indicates the measurement by the authors under the approximate far field conditions outside of 30m from the light channel exit in the experiments, with respect to the results of

the time-dependent ratio between the thermal-blooming light-beam divergence angle and the laboratory light-beam diffraction angle. We can see that in the beginning instant of thermal blooming, the light-beam divergence angle due to the thermal blooming effect is nearly eight times greater than the diffraction angle. The result is basically consistent with the conclusion when the authors calculated under the conditions of the corresponding parameter N, that there is one order of magnitude in the ratio between the divergence angle and the diffraction angle of the far field propagation after the laser beam passes through the absorption layers [6]. When t>200ms, with the disappearance of the thermal lens, the divergence angle of the light beam tends to approach the diffraction angle. This is also consistent with our theoretical analysis.

The first draft of the paper was received on January 25, 1991; the final revised draft was received for publication on April 16, 1991.

DISTRIBUTION LIST

DISTRIBUTION DIRECT TO RECIPIENT

ORGANIZATION	MICROFICHE
BO85 DIA/RTS-2FI	1
C509 BALL0C509 BALLISTIC RES LAB	1
C510 R&T LABS/AVEADCOM	1
C513 ARRADCOM	1
C535 AVRADCOM/TSARCOM	1
C539 TRASANA	1
Q592 FSTC	4
Q619 MSIC REDSTONE	1
Q008 NTIC	1
Q043 AFMIC-IS	1
E404 AEDC/DOF	1
E410 AFDTC/IN	1
E429 SD/IND	1
P005 DOE/ISA/DDI	1
1051 AFIT/LDE	1
PO90 NSA/CDB	1

Microfiche Nbr: FTD96C000364
NAIC-ID(RS)T-0137-96